Seasonal variations of gravity wave activity and spectra derived from sodium temperature lidar

Guotao Yang,[1] Barclay Clemesha,[1] Paulo Batista,[1] and Dale Simonich[1]

[1] Gravity wave measurements were carried out by a newly developed sodium temperature lidar at São José dos Campos (23°S, 46°W). The seasonal variations of gravity wave activity and spectra derived from temperature data are investigated. The total temperature perturbation and temperature vertical power spectra, Ft(m) at $2\pi/(8\text{ km})$, $2\pi/(4\text{ km})$, and $2\pi/(2\text{ km})$ all show that the semiannual maxima occur near the equinoxes, which is consistent with our earlier study (Yang et al., 2006) using only sodium concentration data. The vertical structure of the mean temperature variance could be related to the vertical distribution of N^2. Large nightly variability of the temperature perturbation spectral slope was also found as in other sodium concentration lidar studies. The comparison between temperature and density perturbations induced by quasi-random waves was investigated, and the agreement was found to be good on most (~78%) nights. Good agreement between monochromatic wave-induced temperature perturbations and sodium concentration perturbations has also been found, and the wave parameters derived from temperature data and sodium concentration data are comparable.

1. Introduction

[2] Gravity waves have great influence on the circulation, structure, and composition of the middle and upper atmosphere. Gravity wave observations can provide information on geographical and temporal variations in gravity wave activity and characteristics. But there are conflicting sets of observations that sometimes agree with one another and other times do not [*Fritts and Alexander*, 2003].

[3] Sodium lidar is a useful tool for studying gravity waves in the mesopause region. Previous lidar studies have concentrated on measuring quasi-monochromatic wave characteristics, since monochromatic wave perturbations can be seen clearly from lidar profiles or on calculation of quasi-random wave variances and spectra, as most of the observed wave perturbation is associated with random wave motions [*Gardner and Voelz*, 1987; *Senft and Gardner*, 1991; *Beatty et al.*, 1992; *Collins et al.*, 1994, 1996; *Yang et al.*, 2006, 2008a].

[4] In the 1990s, sodium temperature lidar and later sodium temperature/wind lidar were developed. As sodium density, temperature, and winds are obtained simultaneously, many phenomena associated with gravity wave propagation processes, such as wave damping, overturning, breaking, or instability production have been reported [*Swenson et al.*, 2003; *Xu et al.*, 2006; *Franke and Collins*, 2003; *Li et al.*, 2007; *Williams et al.*, 2002]. Vertical heat fluxes induced by dissipating gravity waves have also been derived from temperature/wind lidar data [*Liu and Gardner*, 2005; *Gardner and Liu*, 2007].

[5] Most temperature/wind lidar studies have focused on gravity wave saturation and dissipation processes, as these have a large effect on the atmospheric energy cycle. However, the observations of gravity wave characteristics, perturbation, and spectra are also important, and temperature/wind lidar studies of these topics are few. In different latitudes/locations, the seasonal maxima and minima of gravity wave activity are observed on different days, and the different seasonal variation of gravity wave activity may reflect the local dynamics processes related to gravity waves. But temperature/wind lidar studies about this topic are rare: Through the Na temperature/wind lidar at Kirtland Air Force Base (35°N, 106.5°W), *Gardner and Liu* [2007] found that the seasonal maxima of temperature and wind variances are around the solstices. The "universal" atmospheric spectrum reported by *Vanzandt* [1982] has stimulated interest. Several theories have been proposed to explain this phenomenon, and many observations of the atmospheric spectrum have been made using different detection tools. But information on the gravity wave spectrum and its seasonal variability does not appear to have been published on the basis of sodium temperature/wind lidar studies.

[6] The atmospheric density perturbation can be derived from sodium concentration fluctuations [*Senft and Gardner*, 1991; *Yang et al.*, 2006], but a number of assumptions must be made. Since sodium concentration and temperature in the same area can be detected simultaneously by sodium temperature/wind lidar, if they are both caused by a gravity

[1]Instituto Nacional de Pesquisas Espaciais, São José dos Campos, Brazil.

Table 1. Annual and Semiannual Components of Gravity Wave Parameters[a]

$\hat{y}$	A0	A1	A2	d1	d2	u1	U2	u1/A1	u2/A2
$\langle ra^2 \rangle^{1/2}$ (%)	3.6	0.1	0.6	51	93	0.14	0.15	1.41	0.255
$Fa(m_8)$ 10^x(m/cyc)	0.08	0.05	0.09	293	104	0.038	0.040	0.756	0.439
$Fa(m_4)$ 10^x(m/cyc)	−0.46	0.06	0.14	329	101	0.032	0.032	0.537	0.227
$Fa(m_2)$ 10^x(m/cyc)	−1.06	0.09	0.19	352	99	0.032	0.032	0.354	0.169
$\langle (dra/dt)^2 \rangle^{1/2}$ (%h)	8.0	2.9	0.7	358	254	0.35	0.15	0.32	0.46

[a]Here u1 (u2) denotes the uncertainty of the amplitude A1 (A2), and $\hat{y}$ = A0 + A1 • cos[(d − d1) • 2π/365] + A2 • cos[(d − d2) • 4π/365]. Note that in the MMSE fit, the logarithms of $Fa(m)$ were taken, so the values (x) of A0, A1, and A2 should be computed as 10^x.

wave perturbation, then the temperature variation should be consistent with that in atmospheric density. However, until now, lidar studies of comparisons between sodium concentration and temperature perturbations are few, although *Collins et al.* [1997] did compare the nightly averaged RMS horizontal wind derived from sodium concentration fluctuations to that derived from the temperature fluctuations. Comparison between the sodium concentration fluctuations and temperature perturbation can test the assumptions for gravity wave analysis from sodium concentration and validate whether the methods for wave measurement are effective.

[7] In this paper, based on temperature measurements made by a newly developed sodium temperature lidar, gravity wave activity, and spectra, as well as their seasonal variations, are derived from lidar temperature data. Detailed comparisons are made between gravity wave perturbations in density and temperature. We also make comparisons between wave parameters derived from density variations and those from temperature variations. The paper is organized as follows: After a brief description of the observations in section 2, studies of gravity wave activity and spectra from temperature data, as well as their seasonal variations, are given in section 3. The first part of this section presents wave-induced perturbations derived from temperature data and their seasonal variations, and the second part presents the spectra of the temperature perturbations and their seasonal variations. Comparisons of wave measurements by density and by temperature fluctuations are given in section 4. The first part of this section presents a comparison of quasi-random wave perturbations in sodium concentration and temperature, and the second part consists of a comparison of monochromatic wave parameters and perturbations derived from sodium concentration and from temperature fluctuations, respectively. Section 5 is the discussion and section 6 is the summary of the results presented in this paper.

2. Observations

[8] Our sodium temperature lidar is located at São José dos Campos (23°S, 46°W). A brief description of the equipment is as follows: The lidar transmitter generates 589 nm pulses by mixing the output of two pulsed neodymium: yttrium/aluminum/garnet (Nd:YAG) lasers, seeded by continuous wave Nd:YAG seeders operating at 1064 and 1319 nm,

respectively. By thermally tuning the seeders it is possible to switch the output wavelength between the sodium D2a resonance peak and the crossover minimum. Temperature is determined by comparing the scattering from the sodium layer at these two wavelengths. The transmitter generates pulses of about 50 mJ at 10 pps. The receiver uses a 0.6 m diameter mirror and two photo multiplier tubes to extend the dynamic range. Photon counting with a 2 μs range interval, corresponding to 300 m range resolution, is used to register the return signal, which is calibrated by comparison to the Rayleigh scattering from between 35 and 40 km.

[9] The temperature lidar was first put into operation in March 2007. Since that time, three different operational procedures have been used: In the first stage (March–July 2007), the laser was tuned sequentially to the D2a peak, the crossover resonance, and the D2b peak, the returns from 500 laser shots being accumulated for each wavelength. This process, taking 4.5 min, was repeated continuously and automatically throughout the observation period. In the second stage of operation (August–October 2007), a similar sequence was used, but the D2b wavelength was omitted. The third state of operation used the same wavelengths as the second, but with 250 shots at the D2a wavelength and 750 at D2b. This arrangement was used to give approximately the same photon returns at D2a and at the crossover wavelength. In this configuration, we can make one temperature measurement every 3 min.

[10] The altitude resolution of our sodium temperature lidar is 300 m. We used the data from April 2007 to April 2008 for temperature calculation and gravity wave studies. These data include a total of 51 nights of observations, and the observation time is generally longer than 3 h. More information on the observations is given in Table 1.

[11] The sodium concentration can be derived from the profiles when the laser is tuned to the D2a peak. In calculating the density, the absorption effect of the sodium layer should be considered. As the sodium concentration can vary greatly during laser tuning, large errors can result in the measured temperatures [*She et al.*, 1992]. To decrease this error, we average every 10 D2a sodium concentration profiles into a merged D2a profile. Similarly, every 10 profiles of D2b or crossover resonance are merged to produce a D2b or crossover resonance profile, respectively. Additionally, all the merged profiles are 5 point averaged in height. With the merged profiles of D2a, D2b, and crossover resonance, the sodium temperature can be extracted.

3. Seasonal Variations of Wave-Induced Perturbations and Their Impact on Temperature and the Associated Temperature Spectra

3.1. Wave-Induced Perturbations Derived From Temperature Data and Their Seasonal Variations

[12] To show how the wave-induced perturbations are obtained from the extracted temperature data, we will show one night's observation as an example. Figure 1a shows the observed temperature sequences observed on the night of 23 August 2007. The time interval between these profiles is 30 min. Here, we give all the temperature profiles a sequence number, starting from the left of Figure 1a, and the
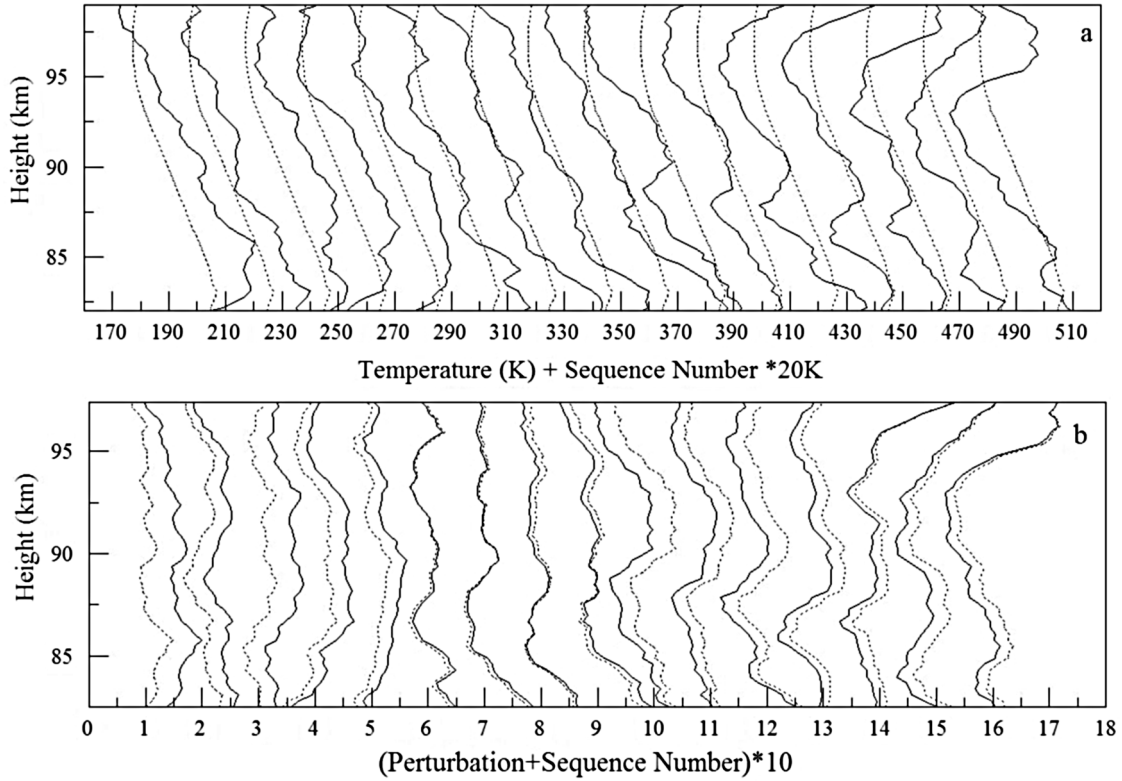
Figure 1. (a) The extracted temperature data sequence (solid curves) on 23 August 2007 at São José dos Campos. The dotted curves are the background temperature. The *x* scale indicates the measured temperature for the first profile, and the other profiles are displaced sequentially by 20 K. (b) The calculated temperature perturbations (solid curves) from the temperature profiles in Figure 1a are 24 km high-pass filtered to produce the final temperature perturbations (dotted curves). The value of the perturbation on the *x* axis is plotted as (perturbation * 10 + sequence number). Here, we give all the temperature profiles a sequence number starting from the left of the panel.

sequence number will be used in Figures 12, 15, and B1a. The *x* scale indicates the measured temperature for the first profile, and other profiles are displaced by 20 K accumulatively. Note that the height range of the measured temperature is smaller than that of the sodium layer. This is because the low sodium concentrations at the edges of the layer lead to excessive temperature errors.

[13] If we believe the temperature perturbations to be mainly caused by gravity wave perturbations, the wave-induced perturbations can be expressed by relative temperature perturbations $rt(z, t)$, which can be calculated directly from the temperature data:

$$rt(z,t) = \frac{\Delta T(z,t)}{T_0(z)} = \frac{T(z,t) - T_0(z)}{T_0(z)} \quad (1)$$

where $T(z, t)$ is observed temperature profile, $T_0(z)$ is the "unperturbed" background temperature profile, and $\Delta T(z, t)$ is the difference between $T(z, t)$ and $T_0(z)$.

[14] There are several methods to determine the background temperature profile for the observation data. Here, we use a simple method: The extracted temperature files are averaged over one observation night and 6 km in height.

The background temperature profile obtained is shown as the dotted curves in Figure 1a.

[15] Once the background temperature profile has been obtained, the temperature perturbations $rt(z, t)$ can be calculated, as shown in the solid curves in Figure 1b. Here, the values actually plotted are the fractional perturbations multiplied by a factor of 10 and incremented by a sequential integer to provide a horizontal displacement between curves. The same procedure is used in Figures 12b, 12c, and 15b. For detrending, these perturbations are high-pass filtered by a 24 km filter, and the filtered perturbations are shown by the dotted curves in Figure 1b. The final temperature perturbations obtained are the wave-induced perturbations in the temperature data.

[16] The mean square temperature perturbations for each observation night are obtained by averaging the obtained perturbations over time and altitude:

$$\left\langle rt(z,t)^2 \right\rangle = \frac{1}{T_{ob}L} \int \int rt(z,t)^2 \, dt \, dz \quad (2)$$

T_{ob} is the total observation time and L is the height range over which temperature is measured. The mean square temperature perturbation for each of the 51 observation nights
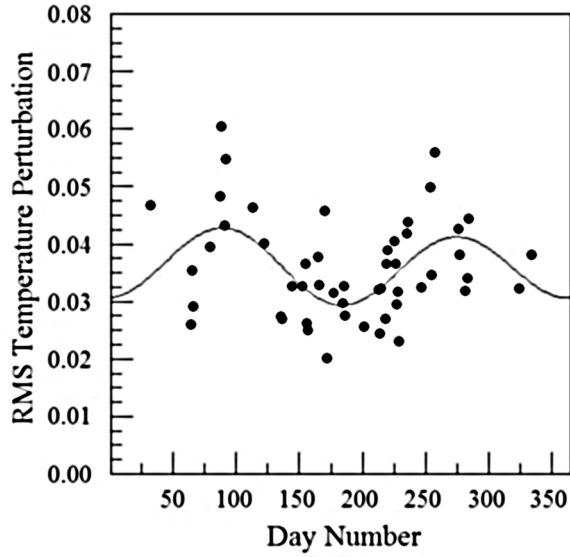
Figure 2. Seasonal variations of the RMS temperature perturbations. The solid curve is a MMSE fit to the atmospheric density perturbation for the mean, annual, and semiannual components.

was calculated, and the seasonal variation of the temperature perturbations was obtained. Figure 2 shows the seasonal variation of the RMS temperature perturbations. These perturbations are induced by gravity waves with periods greater than 30 or 45 min, as temperature is derived from the merged profiles. The effect of the waves with wavelengths longer than 24 km is also removed, as the temperature perturbations are 24 km high-pass filtered. A minimum-mean-square-error (MMSE) fit was made, and the fit parameters are shown in Table 1. From Figure 2 and Table 1, we can see a prominent semiannual variation of gravity wave activity: The magnitudes of the perturbations in March and September are obviously higher than those in December and June, indicating equinoctial maxima in gravity wave activity at our location. The annual variation, maximum at day 51, is much weaker than the semiannual.

[17] Table 1 shows the uncertainties of the fit parameters. In Table 1, u1 (u2) denotes the uncertainty of the amplitude A1 (A2). As in *Yang et al.* [2006], we use the uncertainties (u1 or u2) in the amplitudes (A1 or A2) as compared with the amplitudes themselves as the criterion for judging whether an annual or semiannual variation is significant. We categorize an annual (semiannual) variation as significant when u1/A1 (u2/A2) is lower than 30%, moderately significant when u1/A1 (u2/A2) is between 30% and 40%, weakly significant when u1/A1 (u2/A2) is between 40% and 50%, and insignificant when u1/A1 (ud/A2) is higher than 50%. The semiannual uncertainty (u1/A1) in Figure 2 is only 25.6%, indicating that the semiannual variation of the temperature perturbations is significant, and the annual variation is insignificant as u2/A2 is 141%.

[18] The temperature perturbations $rt(z, t)$ were averaged over the whole observation period for each height to obtain the mean height variation for each night's data. The nightly

means were then used to plot a contour map for the seasonal variation of temperature perturbations as a function of height as shown in Figure 3. Figure 3 shows that the equinoctial maxima in temperature perturbation occur at all heights.

[19] In Figure 4, we show the annual mean height variation of the temperature perturbation. From Figure 4, we can see that the temperature perturbation decreases from 84 to 86 km, remains fairly constant at around 0.03 between 86 and 94 km, and then increases rapidly above 94 km. At 99 km, the upper limit of our measurements, it reaches a value of 0.07.

[20] The convective or static stability of the atmosphere is characterized by the square of the buoyancy frequency N defined as:

$$N^2 = \frac{g}{T}\left(\frac{\partial T}{\partial z} + \frac{g}{C_p}\right) \tag{3}$$

where g is the gravitational acceleration and C_p is the specific heat at constant pressure. When N^2 is negative, the atmosphere is statically unstable.

[21] N^2 was averaged over the whole observation period for each height, and the variation of N^2 with height for each observation night was obtained. Figure 5 shows a contour plot of the seasonal variation of N^2. From Figure 5, we can see that the atmosphere is statically stable throughout the mesopause region. However, near 90 km, two maxima of N^2 occur around the equinoxes, and N^2 around winter solstice is obviously lower than around equinox. It can also be seen that N^2 on the top side of the sodium layer is generally higher that at lower heights.

[22] The annual mean of N^2 as a function of height is shown in Figure 6. From Figure 6, we can see that N^2 increases from 84 km to a maximum at 90 km. It then decreases to a minimum around 95 km. Finally, it increases monotonically throughout the remainder of the height range reaching a maximum value of 0.00057 at 100 km.
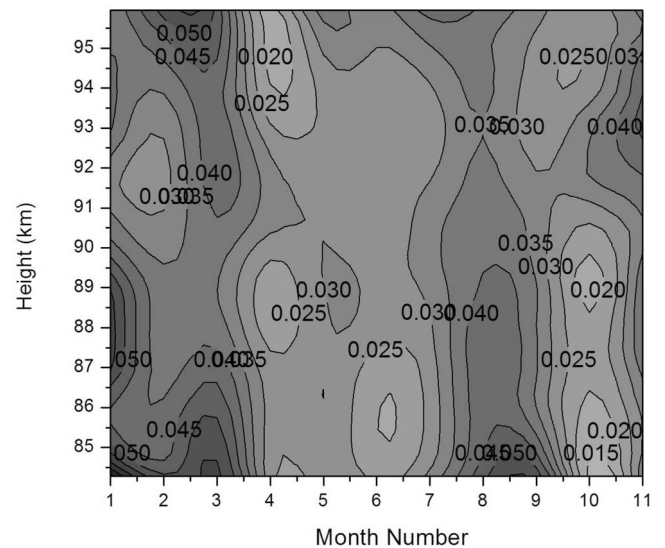

Figure 3. Seasonal variations of relative temperature perturbations versus height and month.
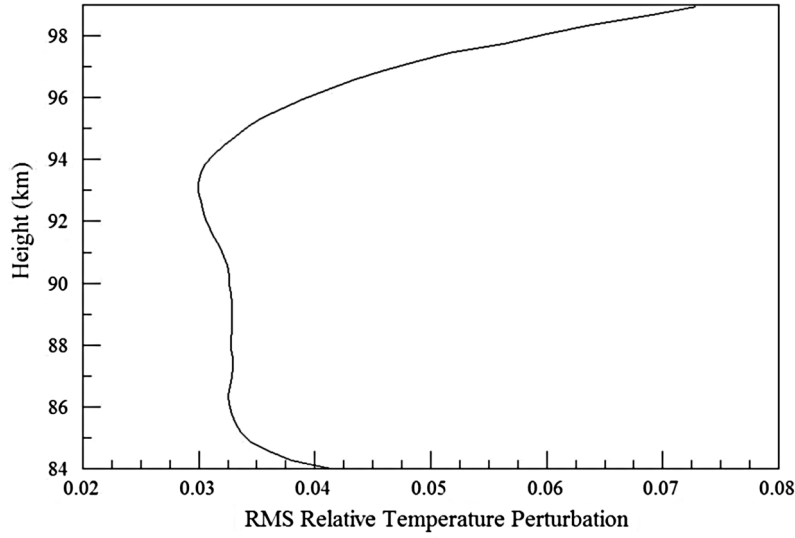
Figure 4. The annual mean profile for relative temperature perturbations versus height.

3.2. Vertical Wave Number Power Spectra of the Temperature Perturbations and Their Seasonal Variations

[23] The vertical wave number power spectrum of the temperature perturbations, $Ft(m)$, gives the contribution of gravity waves with different vertical wavelengths to the temperature perturbations. It can be obtained by:

$$Ft(m) = \frac{\left\langle |Rt(m, t)|^2 \right\rangle}{L} \quad (4)$$

[24] Here, Rt is the vertical Fourier transform of $rt(z, t)$: $Rt(m, t) = \int rt(z, t) * e^{imz} dz$. As in the work of *Yang et al.* [2006], we first prewhiten the temperature perturbations $rt(z, t)$: $y(z, t) = rt(z, t) - 0.95rt(z, t)$. After Fourier transforming,

$Ft(m)$ is obtained by using a recoloring process. This procedure is similar to the high-frequency enhancement used by *Senft and Gardner* [1991]. As pointed out by these workers (see their Figure A1) the high-frequency part of the spectrum will be artificially enhanced if this is not done.

[25] The $Ft(m)$ for each night is obtained by arithmetically averaging $Ft(m)$ from each single data profile. In Figure 7, the solid curves are four examples of the vertical wave number power spectra of the temperature perturbations for four different nights. The data are plotted as single-sided spectra of temperature perturbations in units of $K^2 \cdot$ m/cycle. To estimate the errors caused by photon noise for the spectra, we can use a method similar to that used by *Senft and Gardner* [1991]. When using this method, the photon noise bias needs to be determined. Here, we can assume that
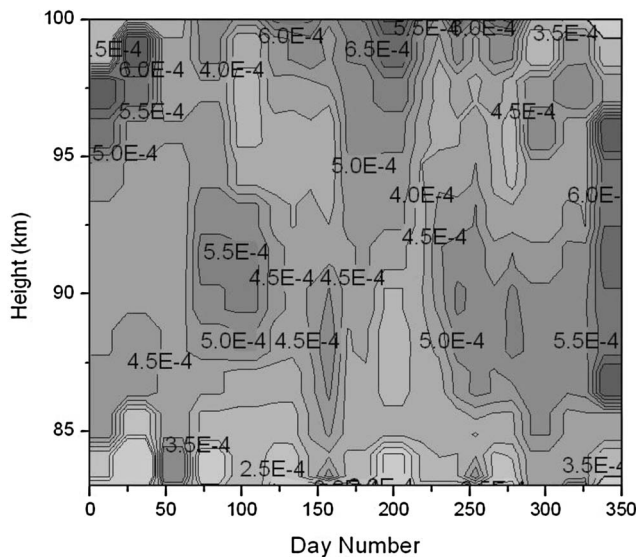

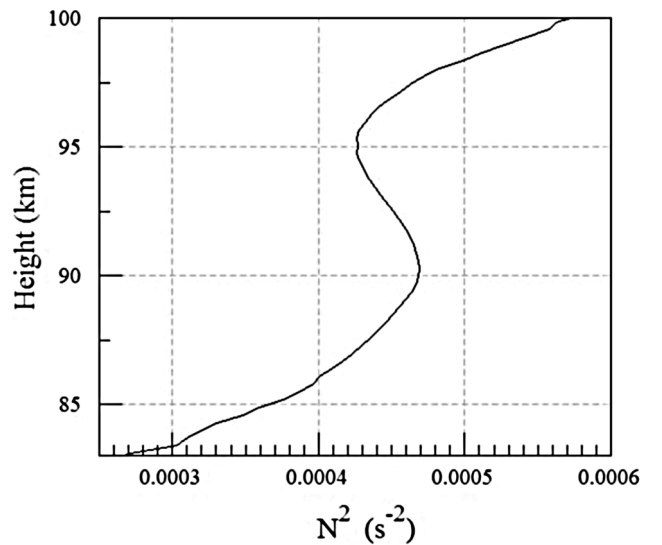**Figure 5.** Contour plot of N^2 versus day number and height.

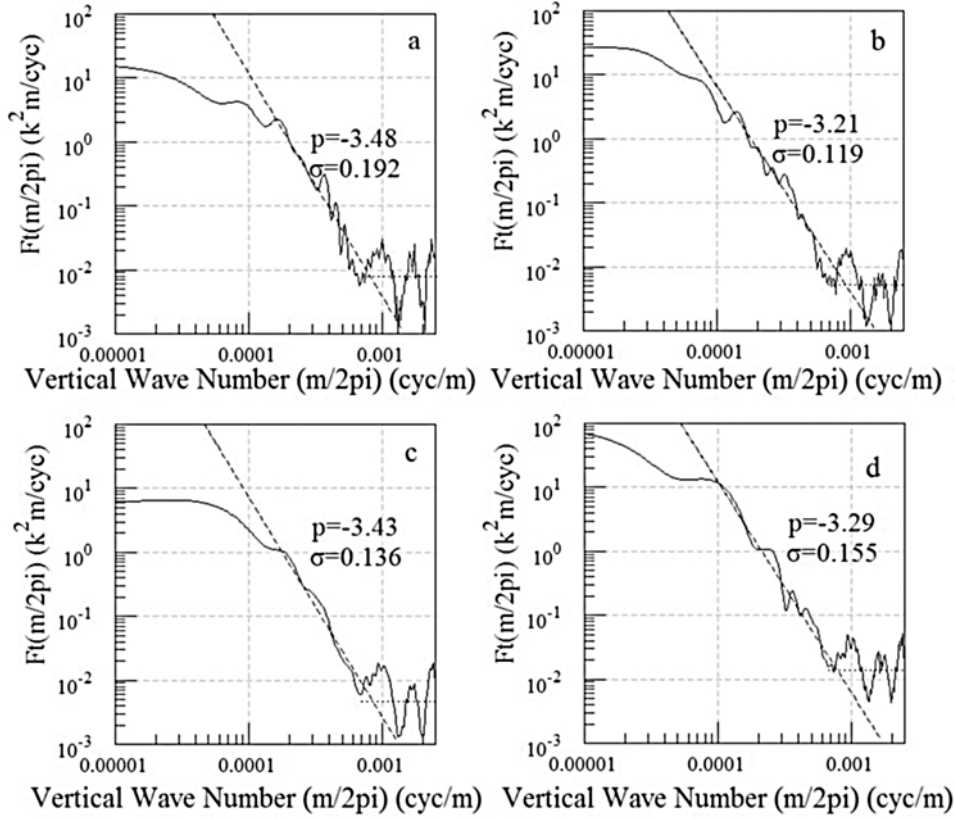**Figure 6.** The average N^2 profile for all the 51 observation nights.

Figure 7. Vertical wave number power spectra of temperature perturbations associated with gravity waves in the mesopause region. The spectra were inferred from temperature data for the nights of (a) 5 March 2008, (b) 8 August 2007, (c) 16 August 2007, and (d) 14 September 2007. The straight dashed lines are the regression fits to the spectra for vertical wavelengths from 2 to 7 km. The dotted lines indicate the photon noise floors, which were subtracted before calculating the slopes. The slopes p and the standard deviations σ for the fit are also given.

the photon noise bias in Figure 7 is approximately equal to that in Figure 6 in the work of *Yang et al.* [2006], as the noise levels in these two groups of figures are similar. Thus, the errors caused by photon noise for the spectra obtained are similar to those in *Yang et al.* [2006]: $Ft(m)$ for $m_8 = 2\pi/(8 \text{ km})$ is 3.7%, $m_4 = 2\pi/(4 \text{ km})$ is 8.0%, $m_2 = 2\pi/(2 \text{ km})$ is 18%, and the nightly mean $\langle rt^2 \rangle$ is 2.4%. The dotted lines indicate the photon noise floors which were subtracted before calculating the slopes.

[26] The spectral slope can be obtained by a linear regression fit to the spectra:

$$\log 10(A) = C + p \bullet \log 10(\omega_v) \qquad (5)$$

while p is the spectral slope, A is amplitude of the spectrum, C is a constant, and ω_v is the vertical wave number.

[27] Here, we also use a MMSE fit for formula (5) to get the fitted line. From Figure 7, we can see that the amplitude at about 1.5 km is closed to the noise level and the perturbations higher than 10 km will be distorted by the limited sodium layer thickness (We will discuss this in Appendix A). So the MMSE fit was made for the vertical wavelength range of 2 to 7 km. The standard deviation σ

between the obtained spectra and the line fit can be used to estimate the uncertainty of the slope, which is calculated by:

$$\sigma = \sqrt{\frac{\sum \left[\log 10(A_o) - \log 10(A_f)\right]^2}{n - 1}} \qquad (6)$$

where A_o and A_f are the amplitudes of the obtained spectra and the line fit for the vertical wavelength range 2–7 km, respectively, and n is the total number of points used in the fit.

[28] The dotted curves in Figure 7 are the line fits for the obtained spectra. The slope p and the standard deviation σ for each example are also given.

[29] Figure 8 shows the seasonal distribution of temperature perturbation spectral slope. The shallowest slope is -1.74 and the steepest is -4.68, while the average value is -3.08. From Figure 8, we can see that the slope of $Ft(m)$ varies greatly from night to night. This large nightly variability was also reported by other workers for sodium concentration data [*Senft and Gardner*, 1991; *Yang et al.*, 2006].

[30] Mean vertical wave number power spectra are shown in Figure 9 for the four 3-month periods centered on the fall equinox, winter solstice, spring equinox, and summer sol-
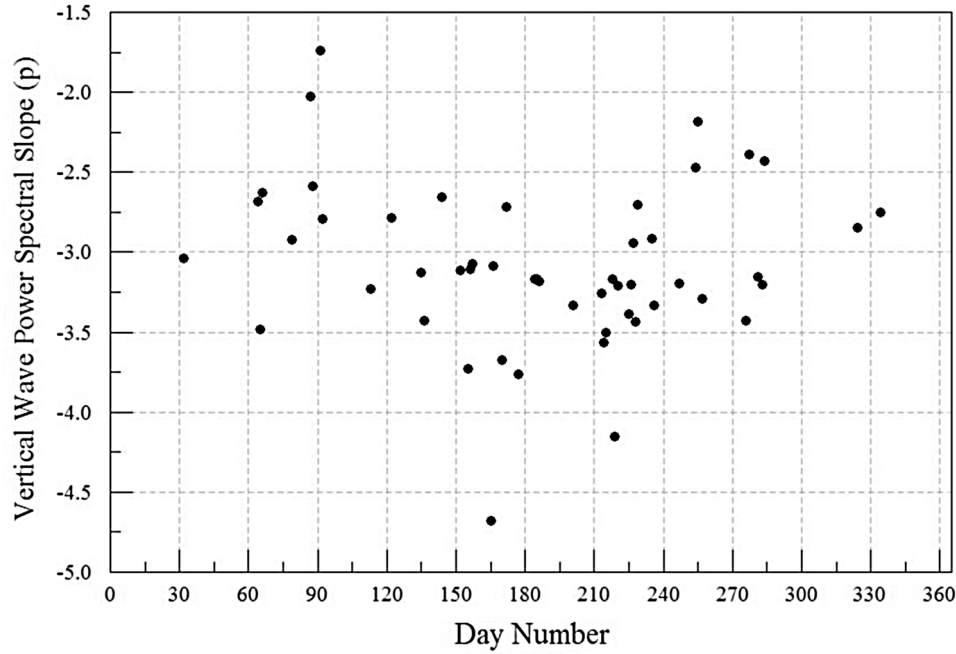
Figure 8. Seasonal distribution of power law slopes for the vertical wave number spectra of the temperature perturbations.

stice. Here, to facilitate comparison with the vertical power spectrum for atmospheric density perturbations, we use the relative temperature perturbation spectra instead of absolute temperature perturbation spectra, and the unit changes to m/cycle. The slope p and the standard deviation σ for each mean spectrum are also given. $Ft(m_4)$ for $m_4 = 2\pi/(4 \text{ km})$ in all these four 3-month periods are also given in Figure 9. From Figure 9, we can see that the spectrum around winter solstice is lower than that around the equinoxes. This also indicates that the seasonal maxima of the wave perturbations are around the equinoxes.

[31] The annual mean vertical wave power spectrum of the temperature perturbations is given in Figure 10. A straight line fit to this spectrum gives a slope of −3.01, consistent with the value of −3 predicted by both the linear instability theory [*Dewan and Good*, 1986] and by the Doppler-spreading theory of *Hines* [1991].

[32] The seasonal variations of $Ft(m)$ for $m_8 = 2\pi/(8 \text{ km})$, $m_4 = 2\pi/(4 \text{ km})$ and $m_2 = 2\pi/(2 \text{ km})$ are shown in Figure 11. From Figure 11, we can see that all have prominent seasonal variations with maxima near the equinoxes. Three MMSE fits were also made, and the fitting parameters are given in Table 1. In the MMSE fit, the logarithm of $Fa(m)$ was used. The annual mean value of m_8 is 1.20 (m/cycle), and the annual oscillation is much weaker than the semiannual component. Its maximum occurs at day 285. The annual mean value of m_4 is 0.35 (m/cycle), and the annual component is also much weaker than the semiannual component. Its maximum occurs at day 290. The annual mean value of m_2 is 0.087(m/cycle). The annual component and the semiannual component are both prominent, and the maximum occurs at day 292.

[33] The uncertainties of the fit parameters are also given in Table 1. From Table 1, we can see that the semiannual

variation of $Ft(m_8)$ is weakly significant as its u2/A2 is between 40% and 50%, the semiannual variation of $Ft(m_4)$ is significant with u2/A2 at 22.7%, and the semiannual variation of $Ft(m_2)$ is also significant with u2/A2 at 16.9%. The annual variation of $Ft(m_8)$ and $Ft(m_4)$ are insignificant, but the annual variation of $Ft(m_2)$ is moderately significant.

4. Comparisons of Wave Measurements From Temperature and Sodium Concentration Data

[34] For high-frequency ($\omega^2 \gg f^2$, where f is the local inertial frequency) gravity waves, the relative density perturbations are much greater than the relative pressure perturbation so that, under the Boussinesq approximation and the ideal gas law, the density perturbations should be equal to the negative of the temperature perturbations [*Nappo*, 2002; *Yu and She*, 1993; *Collins et al.*, 1997]. The periods of the waves measured by lidar are often only a few hours, and thus the condition for this inverse relationship is fulfilled.

[35] For gravity wave measurements from sodium concentration data, previous studies have developed good fundamental theories and assumptions. Most of these studies were done by Illinois researchers [*Senft and Gardner*, 1991; *Gardner and Voelz*, 1987; *Beatty et al.*, 1992], and these theories and assumptions are summarized in Appendix A. On the basis of the well-established theory of sodium concentration perturbed by gravity waves, many gravity wave measurements have been reported from sodium concentration lidar observations [e.g., *Senft and Gardner*, 1991; *Collins et al.*, 1996; *Yang et al.*, 2006]. However, the fact that the theory is well established does not mean that it should never be tested. Since sodium concentration and temperature in the same area are simultaneously detected by
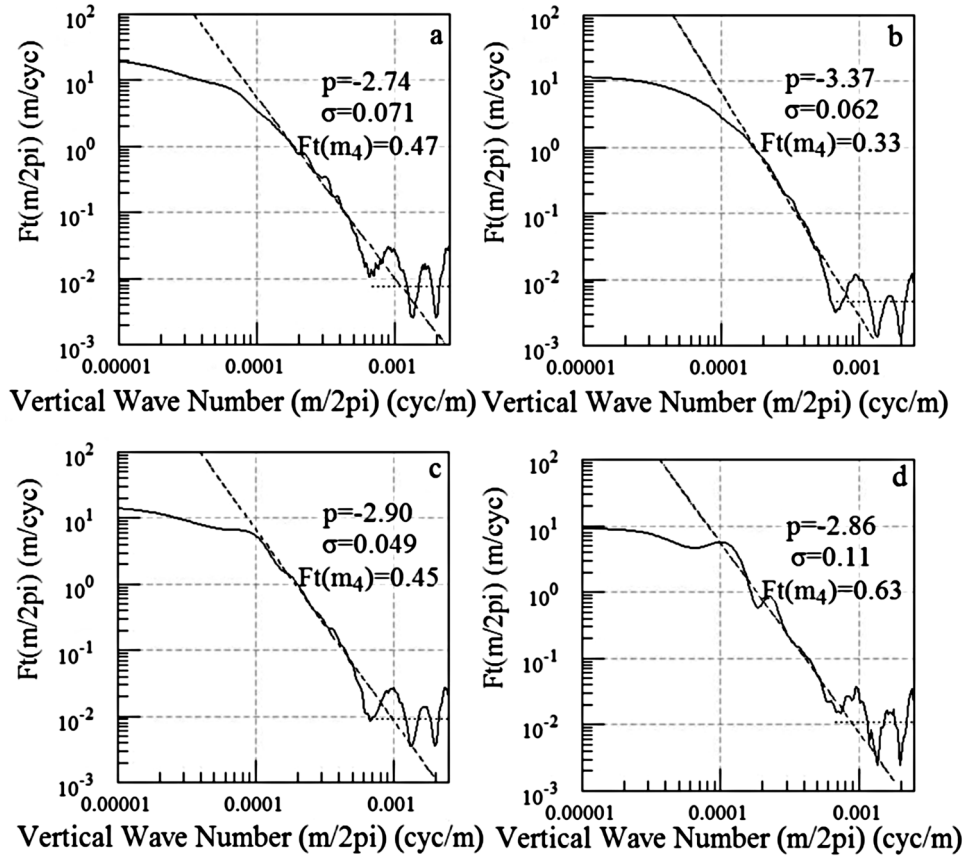
Figure 9. Mean vertical wave number power spectra of the relative temperature perturbations for the four 3-month periods centered on the (a) fall equinox, (b) winter solstice, (c) spring equinox, (d) and summer solstice. The straight dashed lines are the regression fits to the spectra for vertical wavelengths from 2 to 7 km. The dotted lines indicate the photon noise floors, which were subtracted before calculating the slopes. The slopes p and the standard deviations σ for the fit are also given.

sodium temperature lidar, the temperature variation should be consistent with the atmospheric density variation if they are both caused by the gravity wave perturbations. Now that we have simultaneous temperature and sodium concentration observations, we can compare the gravity wave measurements from temperature data and sodium concentration data.

[36] In gravity wave analysis from sodium concentration data, two kinds of wave perturbation have been studied: Quasi-monochromatic wave perturbations, where a quasi-sinusoidal oscillation can be seen in the sodium concentration data, and quasi-random wave perturbations, the more common case, where the sodium concentration is perturbed by multiple waves. We will make comparisons for these two kinds of wave measurement in sections 4.1. and 4.2.

4.1. Comparison of Quasi-random Wave Perturbation in Density and Temperature

[37] Figure 12a shows the observed sodium concentration sequence observed on the night of 23 August 2007. The time interval between these profiles is 30 min. The solid curves are the observed sodium concentration and the dotted curves are the averaged background sodium layer. These sodium concentration profiles correspond to the temperature

profiles shown in Figure 1a. Using the same method as *Yang et al.* [2006], the atmospheric density perturbation for this night can be calculated. The solid curves shown in Figure 12b are the calculated atmospheric density perturbations. The calculated density perturbation becomes unreasonably large a few kilometers above the sodium layer peak, where the density perturbation obtained should be disregarded. From Figure 12b we can see that we have to disregard the density perturbation in the range of 92.5–97.5 km, and only the density perturbations in the ranges 78–92.5 km and 97.5–105 km can be used for comparison. Unfortunately, the measured temperature perturbation in this night (Figure 1b) is effective only at 82.5–97.5 km, so the comparison can only be made for this height range (the bottom side of the sodium layer). The density perturbations obtained are also 24 km high-pass filtered, as shown in the dotted curves in Figure 12b.

[38] The comparison between temperature and density perturbations for the night of 23 August 2007 is shown in Figure 12c. The dotted curves represent temperature perturbations and solid curves represent the density (multiplied by −1, for comparison). From Figure 12c, we can see that the agreement is very good. Although some difference is observed in profiles 4–6, agreement can be seen in most
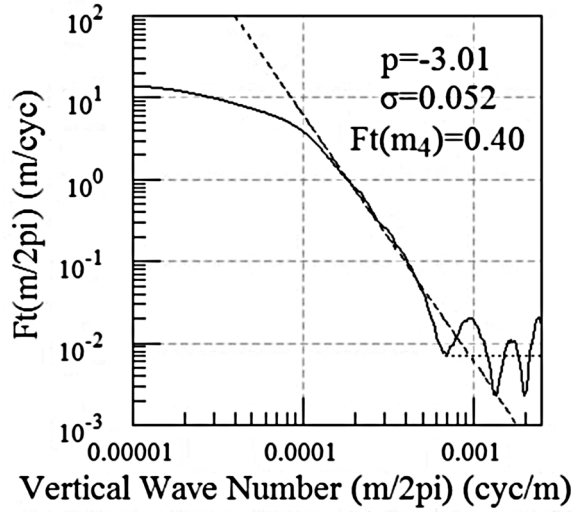
Figure 10. Vertical wave number spectra of the temperature perturbations averaged for all 51 observation nights. The straight dashed lines are the regression fits to the spectra for vertical wavelengths from 2 to 7 km. The dotted lines indicate the photon noise floors, which were subtracted before calculating the slopes. The slopes p and the standard deviations σ for the fit are also given.

profiles, especially 9–14. To provide a quantitative estimate of the difference between the temperature and density perturbations, we use a correlation coefficient C, as:

$$C = \sum_{1}^{N} \left(\frac{\sum_{1}^{M} (ra - \overline{ra}) \bullet (rt - \overline{rt})}{\sqrt{\sum_{1}^{M} (ra - \overline{ra})^2} \bullet \sqrt{\sum_{1}^{M} (rt - \overline{rt})^2}} \right) / N \quad (7)$$

where N is the number of total merged files in the night (16 in this case), M is the number of the height points used for the comparison, ra is the density perturbation ($\overline{ra}$ is its average), and rt is the temperature perturbation ($\overline{rt}$ is its average). For the data shown in Figure 12c, C is 0.77.

[39] The correlation coefficient C, between temperature and density perturbations, is a good parameter for evaluating the comparison, because it represents the degree to which the temperature perturbations approach the density perturbations. We calculated the correlation coefficients for each observation night, and plotted the distribution of C in Figure 13. On two nights, Na_s occurred for most of the observation time, so the comparison cannot be made and the values of C for these nights are not included in the analysis. In calculating C, we estimate that the temperature perturbation corresponds well with the density perturbation when C is higher than 0.60. From Figure 13, we can see that the temperature perturbation corresponds well with the density perturbation on most nights (38 out of a total of 49), as C is greater than 0.6 on about 78% of the observation nights.

[40] The vertical wave number power spectrum of the atmospheric density perturbations, $Fa(m)$, also gives the contribution of gravity waves with different vertical wavelengths to the atmospheric density perturbations. Similarly, it can be obtained by:

$$Fa(m) = \frac{\left\langle |Ra(m, t)|^2 \right\rangle}{L} \quad (8)$$

Here, Ra is the vertical Fourier transform of $ra(z, t)$: $Ra(m, t) = \int ra(z, t)e^{imz}dz$. As there is a gap in the height distribution of $ra(z, t)$, the integral was done only for the bottom side of the sodium layer.

[41] The method for calculating $Fa(m)$ is similar to that used for $Ft(m)$. Mean vertical wave power spectra are shown in Figure 14 for the three 3-month periods centered on the
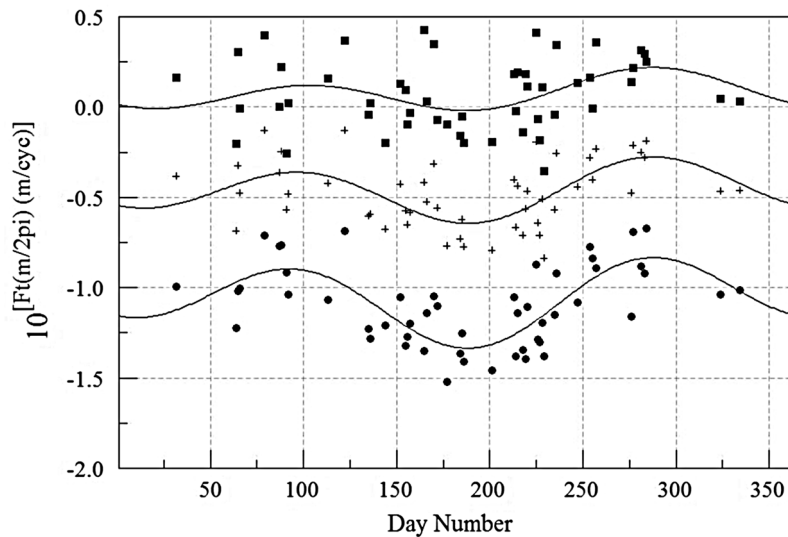

Figure 11. Seasonal distributions of vertical wave number spectral amplitudes for the temperature perturbations at $m8 = 2\pi/(8\ km)$ (circles), $m4 = 2\pi/(4\ km)$ (crosses), and $m2 = 2\pi/(2.5\ km)$ (squares). The solid curves are the MMSE fits for the mean, annual, and semiannual components.
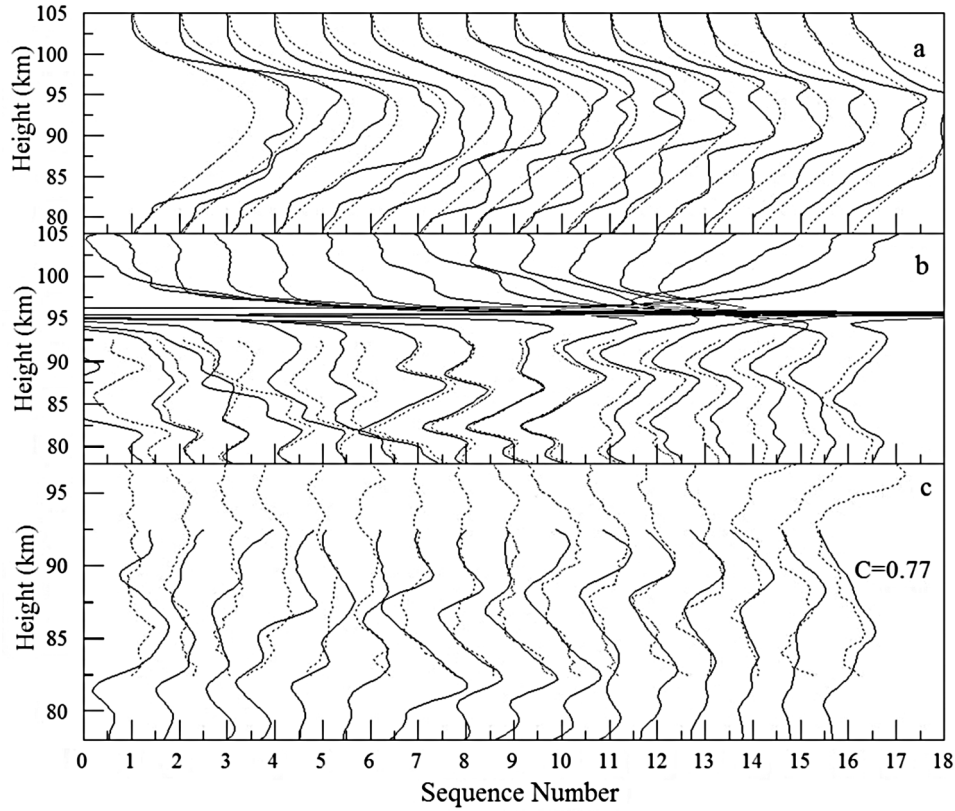
Figure 12. (a) The observed sodium concentration sequence (solid curves) corresponding to that shown in Figure 1a. The dotted curves are the background sodium layer. (b) The calculated atmospheric density perturbations (solid curves) are 24 km high-pass filtered to produce the final density perturbations (dotted curves). (c) Comparisons between temperature perturbations (dotted curves) and density perturbations (solid curves, multiplied by −1), for which the correlation coefficient is 0.77.

fall equinox, winter solstice, and spring equinox, and also the annual mean. We do not show results for summer solstice because we have only two nights of data suitable for calculating the $Fa(m)$ power spectrum for this period. The data used to calculate the summer solstice mean vertical power spectrum in temperature includes three nights, so the spectra extracted from sodium concentration and temperature are not directly comparable as their databases are different. The slope p and the standard deviation σ for each mean spectrum are also given. $Fa(m_4)$ for $m_4 = 2\pi/(4 \text{ km})$ in all these three 3-month periods are also given in Figure 14. From Figure 14 we can see that the spectrum around winter solstice is lower than that around the equinoxes. This also indicates that the seasonal maxima of the wave perturbations are around the equinoxes. The slope in Figure 14a is −2.95, which is a little lower than that in Figure 9a (−2.74). $Fa(m_4)$ in Figure 14a is higher than $Ft(m_4)$ in Figure 9a. Similarly, by comparing the spectral slope p and the amplitude for $m_4 = 2\pi/(4 \text{ km})$ in Figures 9b and 14b, we can see that the slope in Figure 9b is lower than the slope in Figure 14b, and $Fa(m_4)$ is also higher than $Ft(m_4)$. Similar behavior also can be observed by comparing Figures 9c and 12c.

[42] The annual mean vertical wave power spectrum of the density perturbations is given in Figure 14d. A straight line fit to this spectrum gives a slope of −3.29, a little lower than the value of −3.01 for the slope of the annual mean vertical power spectrum of temperature perturbations (shown in Figure 10). $Fa(m4)$ in Figure 14d is 0.54, a little higher than that in Figure 10, so the annual mean vertical power spectrum of the density perturbations is comparable to that of the temperature perturbations.

4.2. Comparison of Quasi-monochromatic Wave Perturbation in Density and Temperature

[43] Sometimes wavelike structures whose peaks and valleys show similar downward velocity are present in sodium data, and this is generally considered to indicate monochromatic wave propagation [e.g., *Gardner and Voelz*, 1987; *Beatty et al.*, 1992; *Yang et al.*, 2008a]. Figure 15a shows the sodium data sequence observed on 7 August 2007. The time interval between these profiles is 30 min. From Figure 15a, we can see structures showing clear downward phase progression, indicating that this is a wave perturbation with a vertical wavelength of ~6 km.

[44] In the work of *Gardner and Voelz* [1987], the wave parameters are extracted from the vertical power spectrum and the background sodium layer is assumed to have an approximately Gaussian shape. *Yang et al.* [2008b] found that the background sodium layer over their site is often far from a single symmetrical Gaussian, so they developed a new method to extract wave parameters. It should be noted
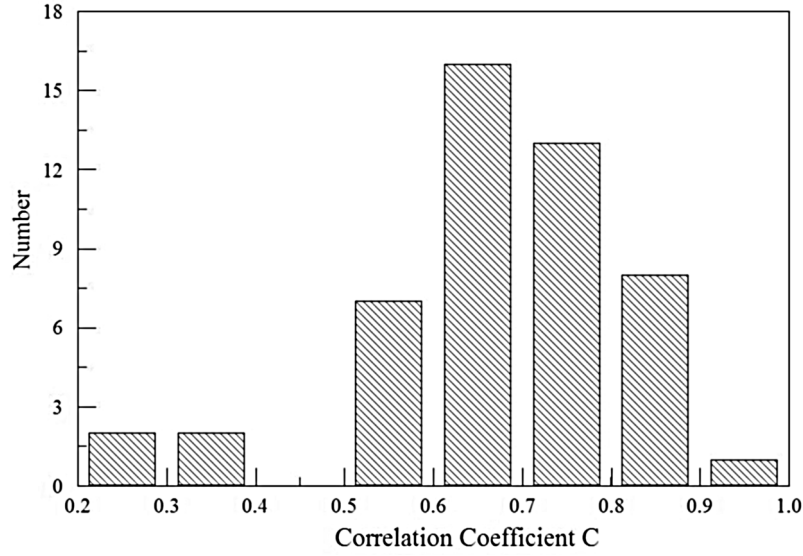
Figure 13. Histogram of the correlation coefficient C obtained for 49 observation nights.

that this work did not invalidate that of *Gardner and Voelz* [1987] when applied to observations with a well-behaved background layer, but the new method, also based on the fundamental theory developed by Gardner and his collea-gues, does give much better results when the background layer is far from Gaussian or in the presence of sporadic layers, which is frequently the case at our location. In this paper, we will use the method developed by *Yang et al.*

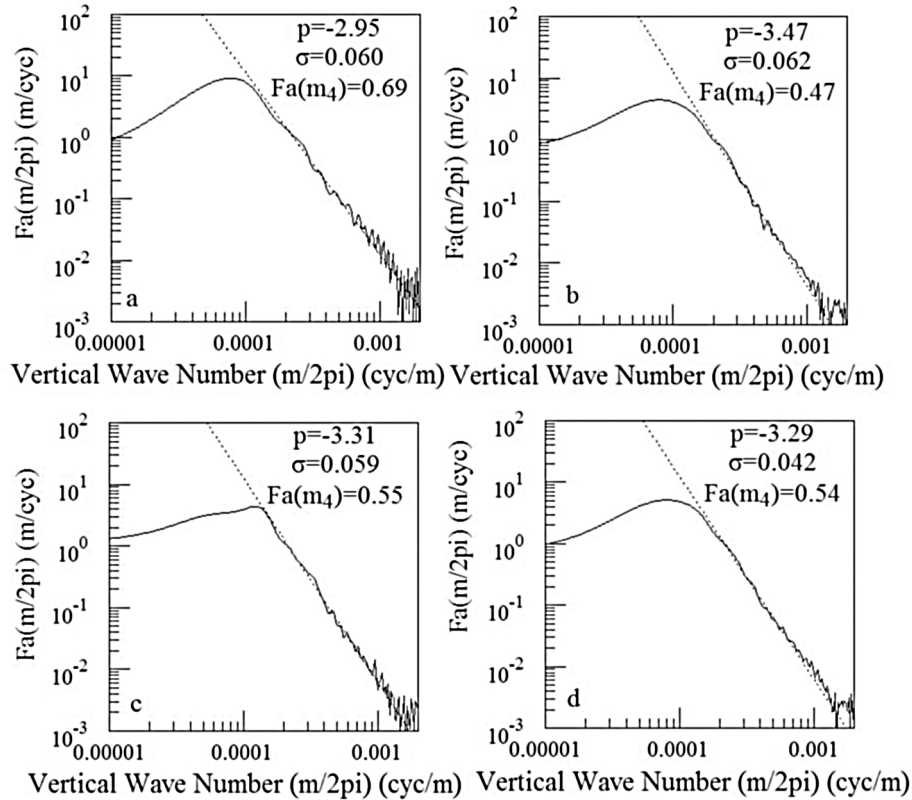**Figure 14.** Mean vertical wave number power spectra of the atmospheric density perturbations for the three 3-month periods centered on the (a) fall equinox, (b) winter solstice, and (c) spring equinox. (d) The average for all 49 observation nights. The straight dotted lines are the regression fits to the spectra for vertical wavelengths from 1.5 to 6 km. The slopes p and the standard deviations σ for the fit are also given.
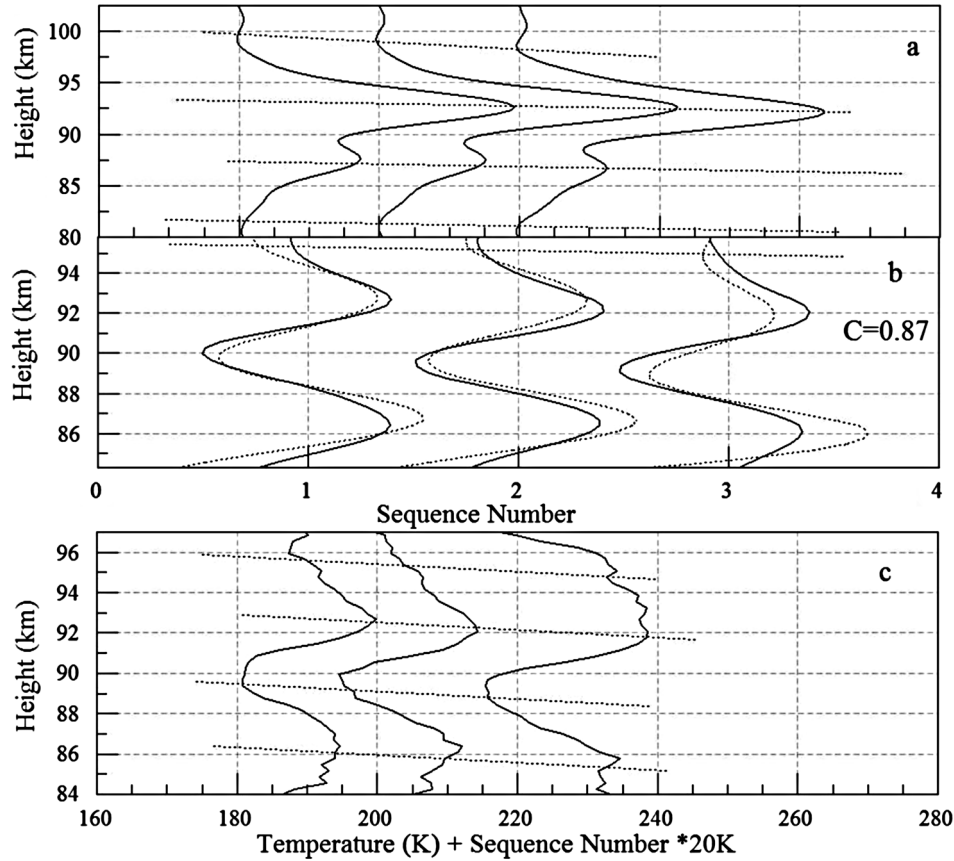
Figure 15. (a) The sodium concentration data sequence observed on 7 August 2007 at São José dos Campos. (b) Comparisons between temperature perturbations (solid curves, multiplied by −1) and density perturbations (dotted curves). (c) The corresponding extracted temperature sequence.

[2008b] to extract wave parameters. The effects of photon noise on the obtained wave parameters were discussed by *Gardner and Voelz* [1987] and *Yang et al.* [2008a]. Here, the errors in vertical wavelength λ_z, amplitude $Ae^{\beta \cdot 90 \text{ km}}$, and amplitude growth factor β are typically about 0.7%, 5%, and 8% or less, respectively. The detailed method and steps of extracting monochromatic wave parameters from sodium concentration data can be found in *Yang et al.* [2008b]. Here, we just give the results of the analysis of the first profile in Figure 15a. The final wave parameters obtained for this profile are: Vertical wavelength $\lambda_z = 5.99$ km, wave amplitude at 90 km $Ae^{\beta \cdot 90 \text{ km}} = 4.21\%$, and growth height $1/\beta = -11.9$ km.

[45] If the wave amplitude is not large, the density perturbation can be expressed by wave parameters: $ra(z, t) = Ae^{\beta \cdot 90 \text{ km}} \cos(2\pi/\lambda_z*z - \Phi)$. Here, Φ is the phase of the perturbation at 90 km, which can be determined from the observed sodium concentration variation.

[46] The simulated density wave perturbations for the sodium profiles shown in Figure 15a are plotted in Figure 15b as dotted curves. As in the comparison of quasi-random wave measurements, we also calculate the correlation coefficient C between density perturbations and temperature perturbations, but since wave parameters have been extracted, vertical wavelength and wave amplitudes from these two data sets are also compared.

[47] Figure 15c shows the temperature profiles corresponding to the densities shown in Figure 15a. From Figure 15c, we can see clear downward phase progression structures, as the dotted lines indicate. A wave perturbation with vertical wavelength near 6 km can also be observed.

[48] Under formula (1), the temperature perturbations in Figure 15c are calculated directly from temperature data. When we calculate the density perturbation, we suppose the sodium layer is only perturbed by one monochromatic wave and use a Levenberg-Marquardt fit to find the most accurate wave parameters and background sodium layer, resulting in the minimum mean square error between the observed and the simulated layers. Obviously, this method neglects longer wave perturbations. Therefore, for comparison with the density perturbation, the temperature perturbation needs to be high-pass filtered. Here, as this is a $\lambda_z \sim$ 6 km wave, the temperature perturbation was high-pass filtered with a cutoff of 10 km. Moreover, although the temperature profile is extracted from merged density profiles, it still contains many short period variations produced by the temperature extraction process. Therefore, the temperature perturbation was again low-pass filtered with a cutoff of 2.5 km.

[49] The final obtained temperature perturbations are compared to the density perturbations. Before making the comparison we multiply the temperature perturbations by −1.
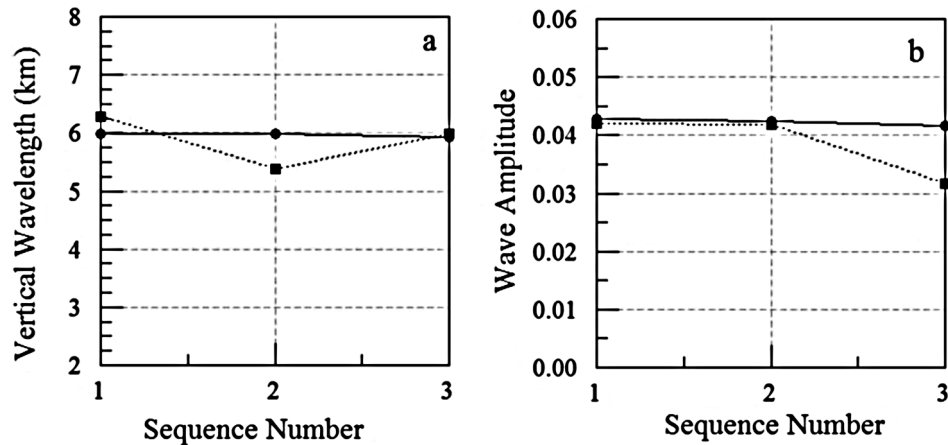
Figure 16. (a) The comparison between vertical wavelengths derived from temperature data (circles) and sodium concentration (squares). (b) The comparison between wave amplitude (at 90 km) derived from temperature data (circles) and sodium concentration (squares).

Comparisons between temperature and density perturbations for this night are shown in Figure 15b, in which the solid curves are temperature perturbations (multiplied by −1) and the dotted curves are density perturbations. Although there are detailed differences, in general the density/temperature curves agree well, and their averaged correlation coefficient C is as high as 0.87. Such good correspondence between temperature and density perturbations induced by a single monochromatic wave does not appear to have been reported in other temperature lidar studies.

[50] The wave parameters can also be obtained from the temperature perturbation. The method is the same as that used by *Yang et al.* [2008b, section 4.4.3]: The vertical wavelength can be estimated by the average distance between the adjacent peaks or valleys of the wave perturbation. The wave amplitude and growth factor can be obtained by making a linear fit to the wave perturbation peaks and valleys. The detailed process can be seen in the work of *Yang et al.* [2008b]. The uncertainties of the wave amplitude and growth factor can be calculated in a manner similar to that used for the uncertainty estimation for the seasonal variation fit parameters. In analyzing the data, we found the uncertainties of the wave amplitude and growth factor to be generally less than 10%. The uncertainty of the vertical wavelength is very small, as the vertical wavelength was directly estimated from the temperature perturbation.

[51] Figure 16a shows the comparison between vertical wavelengths derived from temperature perturbations (circles) and density perturbations (squares). We can see that these two groups of vertical wavelengths are similar. Figure 16b shows the comparison between wave amplitude (at 90 km) derived from temperature perturbations (circles) and density perturbations (squares), again very similar. We also calculated the standard deviations, σ, of these two parameters. The standard deviation of the vertical wavelengths extracted from both temperature and sodium concentration data is 0.48 km, about 8.0% of the average vertical wavelength (5.97 km), indicating that there is no significant difference between the wavelengths derived for the density and temperature profiles. The standard deviation between the wave amplitudes is 0.0071, about 19% of the average wave amplitude (0.038). So the wave amplitudes extracted from these two kinds of data set are comparable.

[52] Monochromatic waves in both temperature and density were seen on 4 more days. Similar to the above analysis, we also calculated the correlation coefficients C between density perturbations and temperature perturbations for these four nights, and give them in Table 2. From Table 2, we can see that C is very high, as all the five are greater than 70% and four of them greater than 80%, which means the density perturbations correspond to the temperature perturbations very well. The vertical wavelengths and wave

Table 2. Differences Between the Gravity Wave Parameters Extracted From Temperature Data and Sodium Concentration Data

Data	Correlation Coefficient C	Standard Deviation σ_{λ_z} of Vertical Wavelength λ_z (km)	Standard Deviation σ_A of Wave Amplitude	σ_{λ_z} Compared With the Averaged λ_z (%)	σ_A Compared With the Averaged Wave Amplitude (%)
7 Aug 2007	0.89	0.48	0.0071	8.0	18.5
24 Aug 2007	0.76	0.78	0.017	11.1	31.9
11 Sep 2007	0.82	0.91	0.012	16.6	41.1
12 Sep 2007	0.86	0.64	0.017	5.2	27.4
14 Sep 2007	0.86	1.17	0.015	10.2	31.2

amplitudes are also extracted for each night both for temperature and sodium concentration. Also, the standard deviations for these two groups of wave parameters were calculated for each night and are given in Table 2. The ratios between the standard deviations and the average parameters are also given in Table 2. From Table 2, we can see that the vertical wavelengths extracted from sodium concentration data correspond well with those obtained from temperature data: The maximum ratio $\sigma_{\lambda_z}/\lambda_z$ is 16.6% and the minimum is only 5.2% while the average is just 10%. The ratio of σ_A to the averaged wave amplitude is somewhat higher: The maximum is 41.1% and the minimum is 18.5% while the average is 30%. Although the difference between the derived wave amplitudes is a bit high, the wave amplitudes extracted from both data sets are comparable.

5. Discussion

5.1. Seasonal Variations of Gravity Wave Perturbations and the Associated Spectra

[53] We have measured the seasonal variation of gravity wave perturbations and the associated spectra at 23°S from the temperature data. The nightly mean square temperature perturbations, the vertical wave power spectral amplitudes at $2\pi/(8\ km)$, $2\pi/(4\ km)$, and $2\pi/(2\ km)$ all show that the semiannual maxima occur near the equinoxes. Moreover, from Figure 9, we can see that the mean vertical wave power spectral amplitude around winter solstice is lower than that around equinoxes. All these measurements indicate that the maxima of the gravity wave perturbation occur near the equinoxes over our site.

[54] *Gardner and Liu* [2007] also reported the seasonal variation of gravity wave perturbations by using a sodium temperature/wind lidar at Starfire Optical Range (35°N). From their Table 1, the RMS annual mean temperature perturbation is 7.9 K. For comparison with density perturbation, we did not calculate absolute temperature perturbation, but calculated the relative temperature perturbation, and the RMS annual mean value is 3.6%. However, if we assume the annual mean temperature at our site is about 200 k, the relative value 3.6% will correspond to absolute value 7.2 K, which compares well with the value of 7.9 K obtained by *Gardner and Liu* [2007].

[55] However, *Gardner and Liu* [2007] found that the wind and temperature perturbations exhibit strong 6 month oscillations with maxima during the summer and winter at 35°N that are about three times larger than the spring and fall minima. This is 3 months out of phase with respect to our measurements since we have found the maxima of the temperature perturbation to be around equinox at 23°S.

[56] Furthermore, there are many reports that found the solstice maxima of gravity wave activity in the mesopause region by using other techniques: At high latitude, *Balsley et al.* [1983] (Fairbanks) using MST radar and *Vincent* [1994] (67°S) using MF radar, all report that the maxima of the gravity wave seasonal variation occur near the solstices. At middle latitude, solstice maxima of gravity wave perturbation were found from sodium concentration lidar data (*Senft and Gardner* [1991], 40°N). *Gavrilov and Jacobi* [2004] using LF D1 wind observations data from Collm, Germany (52°N), found that the gravity wave perturbations maxima occur at the solstices near 83 km, but they shift to the equi-

noxes near and above 100 km. At lower latitude, *Reisin and Scheer* [2004] reported that the maxima in gravity wave activity (from 87 to 95 km) occur at the solstices, using airglow data from E1 Leoncito (31.8°S).

[57] However, at lower latitudes, there are various reports of equinoctial maxima in gravity wave activity in the mesopause region: *Antonita et al.* [2008] found that gravity wave momentum fluxes showed a semiannual variation, with equinoctial maxima and solstice minima, on the basis of meteor radar observations at Trivandrum (8.5°N). From 10 year observations by our previous sodium concentration lidar, *Yang et al.* [2006] reported that the atmospheric density perturbations exhibit large seasonal variation with the maxima occurring near the equinoxes. From the observations of a nearby meteor radar (Cachoeira Paulista, 22.7°S, 45°W), *Clemesha and Batista* [2008] also found that zonal and meridional wind fluctuations show a clear semiannual variation with maxima at the equinoxes, and this result is consistent with that reported by *Yang et al.* [2006]. Moreover, *Clemesha et al.* [2009] found equinoctial maxima in wind fluctuations from two other meteor radar observatories at SJ Cariri (7.3°S, 36.4°W) and Santa Maria (29.7°S, 53.7°W), respectively. The equinoctial maxima of gravity wave perturbation have also been found at northern low latitudes: On the basis of MF radar data from Hawaii (22°N, 160°W), *Gavrilov et al.* [2003] found equinox maxima in gravity wave intensity for heights above 83 km.

[58] The conflicting results for the seasonal variations in gravity wave activity reported by different authors are very interesting. *Gavrilov and Fukao* [1999] use a model to explain the summer maximum of gravity wave amplitude in the mesosphere. From their model, they find that eastward-propagating gravity waves in the troposphere suffer less dissipation in the stratosphere in summer because the stratospheric winds in summer are westward. So the gravity wave amplitude in summer is a maximum in the mesosphere (~70 km), although it is a minimum in the upper troposphere. Similar to this explanation, *Yang et al.* [2006] attributed gravity wave maxima near the equinoxes to the effect of background winds influencing gravity wave propagation and dissipation. They proposed that high-speed zonal winds will change their direction above 90 km in winter, and that the speed is also very high at the inverse direction, so the surviving gravity waves traveling opposite to the mean flow below 90 km will suffer more dissipation as the mean wind change its direction above 90 km, and the same situation will also be present in summer, helping the formation of equinoctial maxima over São José dos Campos. However, there is a lack of experimental evidence for this mechanism.

[59] *Clemesha and Batista* [2008] and *Clemesha et al.* [2009] proposed another mechanism relevant to this problem. They plotted the background wind at 90 km against the fluctuating wind at the same height for the year 2005 at Cachoeira Paulista and found very little correlation between these two parameters. But when they plotted the magnitude of vertical shear of the horizontal winds against the fluctuating wind amplitude for 3 h samples, the correlation coefficient reached 0.45. An even higher correlation coefficient of 0.745 was obtained when using daily mean height-integrated values instead of 3 h samples. These results indicate that the fluctuating wind is closely related to the vertical shear of the horizontal winds. Moreover, it was
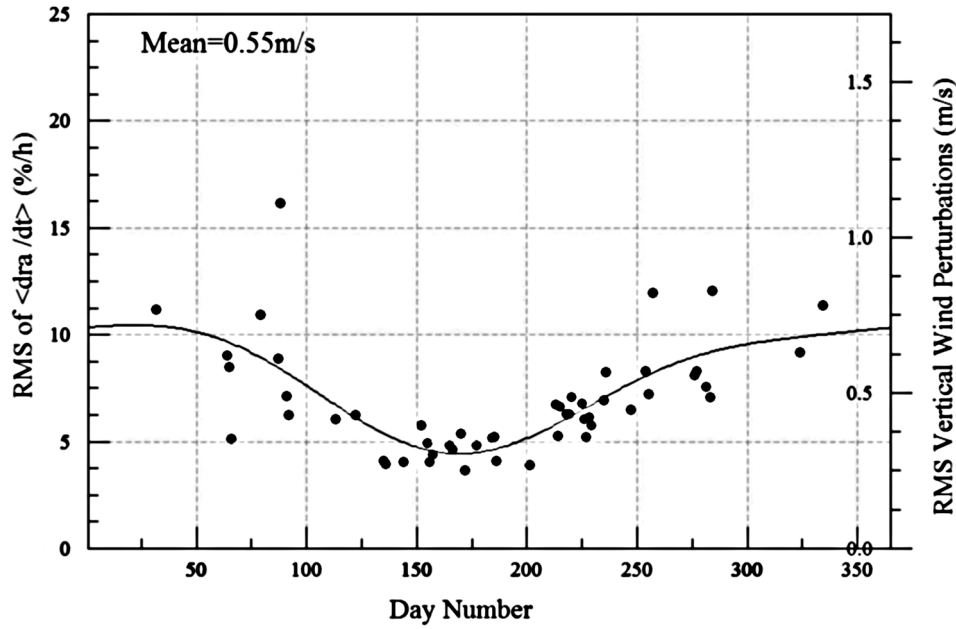
Figure 17. Seasonal distribution of RMS vertical wind perturbations w'_{rms}. The data are scaled for vertical wind on the right-hand axis.

found that the seasonal variation of the fluctuating velocities is similar to that of the wind shear. *Clemesha and Batista* [2008] proposed a novel mechanism to explain this close correlation: In situ wind shear may be a major source of gravity waves and turbulence in the magnetic local time (MLT), explaining the close correlation between the fluctuating wind and the vertical shear of the horizontal winds. This is in contrast to the generally accepted assumption that gravity waves in the MLT are generated at lower heights. This suggestion seems very nonconventional, but it could be a possible explanation for the equinoctial maxima of gravity wave perturbation at our site. Soon a sodium lidar will be installed in Hainan, China, and a meteor radar is also operating at this site. We will compare the gravity wave perturbation detected by lidar and the vertical shear of the horizontal winds to check whether they have a close correlation. However, to test the assumption that gravity waves in the MLT are generated by local vertical shear of the horizontal winds, more atmospheric parameters, both in the MLT and at lower heights, should be measured simultaneously.

[60] From Figure 6, we can see that the annual mean N^2 has a local maximum at 90 km, which is similar to that reported by *Gardner et al.* [2002, Figure 1b] and *Gardner and Liu* [2007, Figure 3b]. N^2 also has a local minimum around 95 km, which is consistent with the findings of *Gardner et al.* [2002] and *Gardner and Liu* [2007]. Above 95 km, N^2 increases rapidly with increasing height, which is also consistent with the work of *Gardner et al.* [2002] and *Gardner and Liu* [2007]. In Figure 4, the temperature perturbations reach a local maximum at 90 km. It then decreases and reaches a minimum near 94 km, subsequently increasing rapidly above this height. Similar results were also obtained by *Gardner et al.* [2002, Figure 5b] and *Gardner and Liu* [2007, Figure 5]. The minimum perturbation is 3%, corresponding to 6 K of absolute temperature perturbation.

This value is again similar to that obtained by *Gardner and Liu* [2007].

[61] *Gardner and Liu* [2007] attributed the vertical structure of the mean temperature variance to the vertical distribution of N^2. They suggest that the vertical structure of the mean temperature variance is related to enhanced wave dissipation where N^2 is low and low dissipation where N^2 is large. *Gardner et al.* [2002] also pointed out that the waves experience severe dissipation in a lower stability background atmosphere (where N^2 is very low) and the wave amplitude increases rapidly above 95 km (where N^2 is largest) as expected in the absence of dissipation.

[62] From Figure 5, we can see that N^2 around the equinoxes is higher than N^2 around the winter solstice, mainly in the 85–95 km region. Similarly, from Figure 3, we can see that the temperature variance around equinoxes is higher than around the winter solstice, especially at heights around 90 km. So under the above supposition, we can relate the maxima of wave activity around the equinoxes to the maxima of N^2 at this time. The lowest value of N^2 around the winter solstice probably indicates that the waves experience severe dissipation, and thus the wave amplitudes are the lowest at this time.

[63] *Senft and Gardner* [1991, Formula 28] indicated that the vertical wind perturbation, w', can be obtained from the temporal derivative variance of the density perturbations:

$$\left\langle \left(\frac{\partial ra}{\partial t} \right)^2 \right\rangle \frac{g^2}{N^4} = \left\langle w'^2 \right\rangle \tag{9}$$

as the density perturbations are equal to the negative of the temperature perturbations. We can calculate w' from temperature perturbations.

[64] Figure 17 shows the seasonal distribution of RMS vertical wind perturbations w'_{rms}. A MMSE fit was also

made. The seasonal distribution of the RMS vertical wind perturbations has a prominent annual variation with a minimum around winter solstice, and the annual uncertainty (u1/A1) is only 12%. The annual mean value of the RMS vertical wind perturbations is 0.55 m/s. These results are comparable to those obtained by *Yang et al.* [2006, Figure 4].

[65] *Senft and Gardner* [1991] indicated that the ratio between the horizontal and vertical path lengths between the source of gravity waves (GW) and the observation site is equal to the ratio between u'_{rms} and w'_{rms}. Here, u' is perturbation velocity and has a relation: $\langle u'^2 \rangle = \langle g/N \rangle^2 \langle ra \rangle^2$. So u' can be calculated from the temperature perturbations. We can get the horizontal distance between the source and our site provided the vertical distance is known. Assuming the sources are in the troposphere, about 90 km below the sodium layer, makes them about 3300 km away from our location. The Andes are about 2200 km from our site, and taking into consideration the fact that our high-pass filtering will tend to increase the distance, it is reasonable to suggest that mountain waves generated by the Andes might be one of the principal sources of the gravity waves detected by our lidar.

[66] *Gardner and Taylor* [1998] pointed out that waves with periods longer than 5 h, vertical wavelengths longer than 15 km, and horizontal wavelengths longer than 1000 km are not presently sampled by lidar data. Moreover, *Gibson-Wilde et al.* [1996] studied the effect of the sodium layer width on the GV87 technique by using a numerical model and found "that quasi-monochromatic gravity waves with vertical wavelengths larger than approximately 10 km may not be reliably retrieved from Na lidar data." However, the range of heights over which temperature can be measured is smaller than that for sodium concentration, and we believe the limit for the longest wave is ~8 km. The limit for the shortest wave is ~1 km, determined by photon noise.

[67] The large nightly variability of the temperature perturbation spectral slope is shown in Figure 8. The slope varies greatly from day to day, and no significant seasonal variation can be seen. This large nightly variability has also been reported by *Senft and Gardner* [1991] and in our earlier paper [*Yang et al.*, 2006], but it is not compatible with the linear instability theory, which suggests that the spectrum goes as m^{-3} if the bandwidth of a wave packet is proportional to m. So the bandwidth of a wave packet must be proportional to m^{q-2}, if the slope q is not equal to 3. The bandwidth dependence in our results ranges from $m^{-0.36}$ to $m^{2.68}$ and changes dramatically from night to night. These extreme night-to-night changes are unexpected.

[68] However, as *Senft and Gardner* [1991] pointed out, the observed slope variability appears to be compatible with the Doppler-spreading theory [*Hines*, 1991]. The slope predicted by the Hines theory depends on the high wave number cutoff of the source spectrum, and the slope variability may be caused by night-to-night changes in this parameter. The observed slope variability is also compatible with the diffusive filtering theory. This theory suggests that a wave of intrinsic frequency ω_i and vertical wave number m will be severely damped when the effective vertical diffusion velocity (mD_{zz}) of particles experiencing the wave motion exceeds the vertical phase velocity of the

wave (ω/m). Thus, only waves satisfying $mD_{zz} \leq \omega/m$ are permitted to grow in amplitude with increasing altitude. The variability of the vertical wave number spectrum slope can be attributed to the variability of the source spectrum slope under diffusive filtering theory.

5.2. Comparisons of Wave Measurements From Temperature Data and Sodium Concentration Data

[69] In addition to Na_s, apparent large production/loss processes or horizontal inhomogeneities in the sodium layer can often be observed in our lidar data, as discussed in Appendix B.

[70] In this paper, the temperatures are measured directly by the technique, and the associated wave parameters derived from the temperatures are therefore relatively straightforward. However, the sodium concentration is affected by the wave motions but also by chemistry and other effects. The wave perturbation and parameters inferred from the sodium concentration is therefore indirect and requires a number of assumptions. The fundamental theory to describe gravity wave perturbations in sodium concentration has been well established by Gardner and his colleagues in Illinois, but this theory also requires several assumptions. As pointed out in Appendix A, these assumptions are (1) there are no chemical effects on the sodium layer related to gravity wave perturbations; (2) the sodium layer is horizontally homogeneous; (3) the diffusion and the chemical effects caused by wave perturbations can be neglected; and (4) apart from chemical effects and horizontal advection, the fluctuations of the sodium layer are mainly caused by gravity wave perturbations.

[71] The first and second assumptions could be satisfied by discarding stretches of data when Na_s and advection are obvious. So we mainly consider the validity of the third and fourth assumptions. *Hickey and Plane* [1995] and *Xu and Smith* [2003] pointed out that the wave-associated chemical effects are not important at most sodium heights. But this result is just obtained from model simulation and needs to be validated by observation. The fourth assumption is just a general assumption and not tested by observation.

[72] However, in gravity wave analysis, the effectiveness of the method and steps are as important as the validity of the fundamental assumptions. Sometimes different methods can result in large differences in the results even though they are implemented under the same fundamental assumptions and theory. In developing the method and steps under the fundamental theory, reasonable methods and steps should be used to carry out the data analysis. These include detrending, removal of short scale fluctuations, determination of the background layer, and so on. Although we try to use reasonable methods and steps to do the data analysis, the effectiveness of the method and individual steps in the process still need to be tested.

[73] We have made a comparison between temperature and density perturbations induced by quasi-random waves and found good agreement in most cases. The comparison is made in height, point by point, profile by profile. We have also made a comparison of quasi-monochromatic wave perturbations in temperature data and sodium concentration data. We found that there to be good agreement between temperature and density perturbations, and the derived wave

parameters from both data sets are comparable, so we think the comparison of quasi-monochromatic wave perturbations is also good. Such a complete comparison between temperature and density perturbations, induced by a monochromatic wave, does not appear to have been reported in other temperature lidar studies.

[74] The good agreement obtained in this paper validates the fundamental assumptions of gravity wave measurements from sodium concentration data, mainly validating the third and fourth assumptions: The diffusion and the chemical effects caused by wave perturbations can be neglected and the fluctuations in sodium concentration are mainly caused by gravity waves. The good agreement also indicates that our method for gravity wave measurements, although it still needs improvement, is effective.

[75] In random gravity wave measurements, although agreement between temperature and density perturbations on most nights is good, large differences are found for about 22% of the nights. The differences might be caused by the temperature error, which is larger at the edge of the sodium layer. Another possibility is that nonlinear perturbations are not effectively avoided when implementing the data analysis.

[76] Some difference also still exists in monochromatic wave measurements, especially the difference between wave amplitudes. The differences also might be caused by the temperature error. Moreover, the method that we used for wave analysis from sodium concentration data may cause some difference. When we extract wave parameters from sodium concentration data, we assume the sodium layer is only perturbed by one wave. So the contributions of other waves with lower amplitude will be neglected, but these contributions are included in the temperature perturbation calculation.

6. Conclusions

[77] We present the seasonal variations of gravity wave perturbation and spectra derived from temperature data. The total temperature perturbations, $Ft(m)$ at $2\pi/(8 \text{ km})$, $2\pi/(4 \text{ km})$, and $2\pi/(2 \text{ km})$, all show that the semiannual maxima occur near the equinoxes, which is consistent with our previous sodium lidar reports [*Yang et al.*, 2006], but is different from the seasonal variation reported by *Gardner and Liu* [2007], also from sodium temperature data. However, although there are many reports that found solstice maxima in gravity wave activity in the mesopause region using other techniques at different latitudes, a number of reports of equinoctial maxima in the mesopause region at lower latitudes can be found in the literature.

[78] We have discussed the possible reasons for seasonal variations in gravity wave activity in the mesopause region, but which, if any, of these is responsible for the equinoctial maxima seen by us is still not clear.

[79] The vertical structure of the mean temperature perturbation could be related to the vertical distribution of N^2, as suggested by *Gardner and Liu* [2007] and *Gardner et al.* [2002]. So we might attribute the maxima of wave activity around the equinoxes to the maxima of N^2 at this time of the year. The temporal derivative variances of the temper-

ature perturbations as well as their seasonal variation were calculated with a minimum around winter solstice. The horizontal distance between GW sources and our site were obtained from the temporal derivative variances of the temperature perturbations, resulting in a mean distance of 3300 km, which could be related to mountain waves generated by the Andes mountains.

[80] The sodium concentration is affected by the wave motions but also by chemistry and other effects. The wave perturbation and parameters inferred from the sodium concentration are therefore indirect and require a number of assumptions, so simultaneous observations of temperature and sodium concentration were used to validate these assumptions. We have made comparisons between temperature and sodium concentration perturbations induced by quasi-random waves. The comparison was made point by point, in height and profile by profile in time. The agreement for most nights is good. On 38 nights out of a total of 49, the correlation coefficient C is higher than 0.6. Comparisons between vertical power spectra for temperature and for density perturbations were also made, and they were also found to be comparable. We have also made a comparison of quasi-monochromatic wave perturbations in temperature and sodium concentration and found good agreement. The good agreement obtained in this paper not only validates the fundamental assumptions of gravity wave measurements from sodium concentration data but also indicates that our earlier procedures for gravity wave measurements from sodium concentration data alone are effective.

Appendix A: Fundamental Theory and Assumptions of Gravity Wave Measurements From Sodium Concentration Data

[81] When the chemical effects on the sodium layer and the horizontal inhomogeneity of the sodium layer are neglected, we can assume that the variations of the sodium layer are mainly caused by gravity wave perturbations. Consequently, atmospheric perturbations, which are directly related to gravity wave perturbations, can be extracted from sodium concentration data. *Senft and Gardner* [1991] have obtained the relation between sodium concentration perturbations and atmospheric density perturbations:

$$rs(z,t) = -\frac{1}{\gamma - 1}\left[1 - \frac{\gamma H(z - z_0)}{\sigma_o^2}\right]ra(z,t) \qquad (A1)$$

where $rs(z, t)$ is the sodium concentration perturbation, $ra(z, t)$ is the atmospheric density perturbation, γ is the ratio of specific heats ($\sim$1.4), z_0 is the center height of the background sodium layer, and σ_0 is the RMS thickness of the background sodium layer.

[82] To derive this relationship, several assumptions are required: There are no chemical effects on the sodium layer related to gravity wave perturbations, the sodium layer is horizontally homogeneous, the diffusion effects caused by wave perturbations can be neglected, the atmospheric density perturbations are just a few percent so nonlinear effects
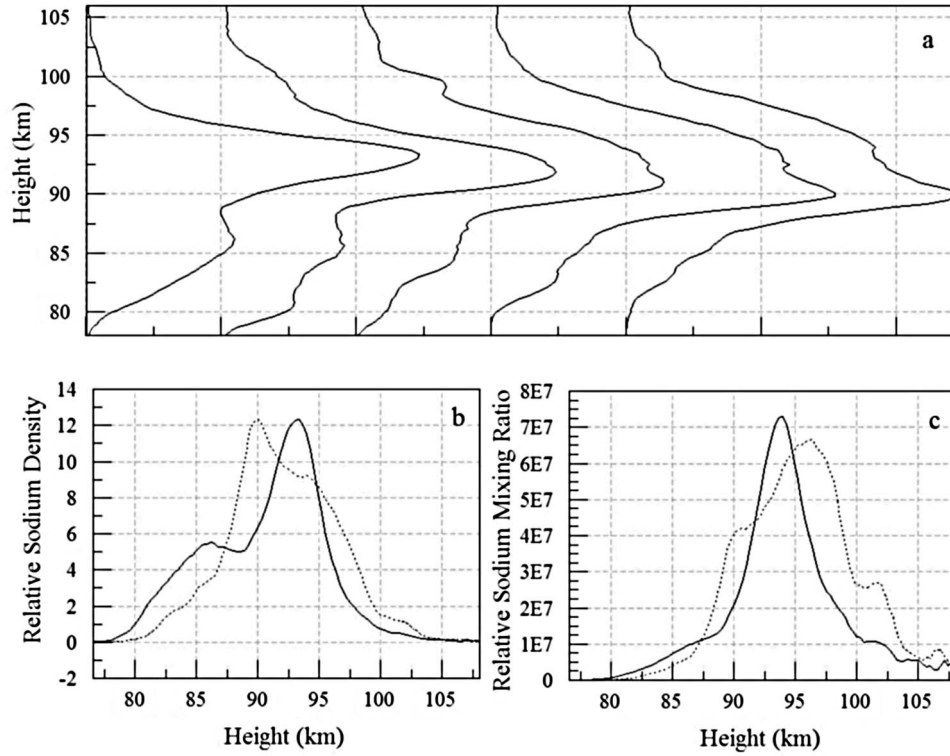
Figure B1. (a) The sodium concentration sequence observed at the night of 9–10 January 2003. (b) The sodium concentrations for the first profile (solid curve) and the fifth profile (dotted curve). (c) The relative sodium mixing ratios for the first profile (solid curve) and the fifth profile (dotted curve).

can be neglected, and the background sodium layer $n_0(z)$ has a Gaussian shape:

$$n_0(z) = \frac{c_0}{\sqrt{2\pi}\sigma_0} e^{-(z-z0)^2/2\sigma_0^2} \tag{A2}$$

where c_0 is the layer column abundance.

[83] To extract atmospheric density perturbations from sodium concentration data, we need to consider these assumptions: Sporadic sodium layers (Na$_s$), which it is difficult to believe to be the result of gravity wave perturbations, are common in our lidar data [*Batista et al.*, 1989]. Moreover, other sodium concentration variations, which are probably caused by sodium layer advection, are not rare in our data set. So we frequently have to discard stretches of data when calculating the sodium variation, but the stretches of data used for density analysis are generally longer than 120 min.

[84] *Senft and Gardner* [1991] have indicated that the diffusion velocity in the mesopause region is very small and can be neglected. *Hickey and Plane* [1995] and *Xu and Smith* [2003] pointed out that the sodium layer is a good tracer for wave perturbations, as the wave associated chemical effects are not very important at most heights (above 85 km).

[85] We can see that the absolute value of the term in square brackets $[1 - \gamma H(z - z0)/\sigma_0^2]$ in formula (A1) will go to 0 near the height $z1 = z0 + \sigma_0^2/\gamma H \sim 94$ km, and this means that nonlinear wave perturbation effects have an important influence on the derived wave parameters around

this height. As a result, it is not possible to get a reliable value of $ra(z, t)$ from $rs(z, t)$ within ±2 km of $z1$ [*Senft and Gardner*, 1991], and the data in this region are not used in our gravity wave analysis.

[86] Our method used to extracted wave perturbations is almost the same as that used by *Senft and Gardner* [1991]. The only difference is that we use the averaged sodium layer (whole observation nights and 6 km average) as the background layer. So the relation between sodium concentration perturbations and atmospheric density perturbations becomes [*Yang et al.*, 2006]:

$$ra(z,t) = -\frac{\gamma - 1}{1 - \gamma H f'(z)} rs(z,t) \tag{A3}$$

where $f'(z) = -n_0(z)/n_0'(z)$.

[87] For monochromatic wave analysis, *Gardner and Voelz* [1987] gave a relation between sodium concentration and gravity wave parameters:

$$n_s(\vec{r},t) = \frac{n_0\left(z - \gamma H \ln\left[1 + [Ae^{\beta z}/(\gamma - 1)]\cos\left(\omega t - \vec{k} \bullet \vec{r}\right)\right]\right)}{\left\{1 + [Ae^{\beta z}/(\gamma - 1)]\cos\left(\omega t - \vec{k} \bullet \vec{r}\right)\right\}} \tag{A4}$$

where $n_s(\vec{r}, t)$ is the sodium layer response to the gravity wave, $n_0(z)$ is the background sodium layer, $Ae^{\beta z}$ is the wave amplitude, β is the amplitude growth factor, ω is the wave frequency, $\vec{r} = x \bullet \hat{x} + z \bullet \hat{z}$ is the position vector

where x is the horizontal coordinate and z is the vertical coordinate, $\vec{k} = k_x \cdot \hat{x} + k_z \cdot \hat{z}$, is the wave number vector, and H is the atmospheric scale height (~6 km).

[88] Assumptions required for derivating equation (8) are almost the same as those of *Senft and Gardner* [1991], except equation (8) has included the nonlinear wave perturbation effects.

Appendix B: A Probable Example for the Horizontal Inhomogeneity of the Sodium Layer

[89] Figure B1a shows the sodium concentration data sequence, observed on the night of 9–10 January 2003. The time interval between these profiles is 15 min. In Figure B1b, the first profile is given by a solid curve and the fifth profile is given by a dotted curve. From Figure B1b, the obvious increase of the sodium concentration at 95–105 km can be observed. We will demonstrate that this variation cannot be caused by gravity wave perturbation.

[90] *Clemesha et al.* [1998] pointed out that if only gravity waves perturb the sodium layer, the mixing ratio of the sodium is conserved while waves obey the nonacceleration conditions and sodium is not chemically active. Here, we just discuss the general case, as sodium variation similar to Figure B1 is often seen at our site. Using a scale height of 6 km for the major constituents, we obtained the sodium mixing ratio profiles plotted in Figure B1c. From Figure B1c, we can see that the sodium mixing ratio increases greatly at 95–105 km. Under the mixing ratio conservation theory, this variation is difficult to account for by a gravity wave perturbation.

[91] The sodium concentration variation on the night of 9–10 January 2003 might be thought of as a chemical effect. But we think it more probable that it is the effect of advection; i.e., this variation is probably caused by the horizontal transport of a sodium concentration gradient. This sort of data sequence will produce a large error in gravity wave analysis, mainly around 100 km, so, in practice, we will disregard such sequences on the basis that the sodium layer is not horizontally homogeneous. The variation of the sodium mixing ratio can be used to distinguish these phenomena when doing data analysis.

References

Antonita, T. M., G. Ramkumar, K. K. Kumar, and V. Deepa (2008), Meteor wind radar observations of gravity wave momentum fluxes and their forcing toward the Mesospheric Semiannual Oscillation, *J. Geophys. Res.*, *113*, D10115, doi:10.1029/2007JD009089.

Balsley, B. B., W. L. Ecklund, and D. C. Fritts (1983), VHF echoes from the high-latitude mesosphere and lower thermosphere: Observations and interpretations, *J. Atmos. Sci.*, *40*, 2451–2466.

Batista, P. P., B. R. Clemesha, I. S. Batista, and D. M. Simonich (1989), Characteristics of the sporadic sodium layers observed at 23°S, *J. Geophys. Res.*, *94*, 15,349–15,358.

Beatty, T. J., C. A. Hostetler, and C. S. Gardner (1992), Lidar observations of gravity wave and their spectra near the mesopause and stratopause at Arecibo, *J. Atmos. Sci.*, *49*, 477–496.

Clemesha, B. R., and P. P. Batista (2008), Gravity waves and wind-shear in the MLT at 23°S, *Adv. Space Res.*, *41*, 1472–1477, doi:10.1016/j.asr.2007.03.085.

Clemesha, B. R., P. P. Batista, and D. M. Simonich (1998), Vertical structure in the topside sodium layer, *Geophys. Res. Lett.*, *25*, 3305–3308.

Clemesha, B. R., P. P. Batista, R. A. B. da Costa, and N. Schuch (2009), Seasonal variations in gravity wave activity at three locations in Brazil, *Ann. Geophys.*, *27*, 1059–1065.

Collins, R. L., A. Nomura, and C. S. Gardner (1994), Gravity waves in the upper mesosphere over Antarctica: Lidar observations at the South Pole and Syowa, *J. Geophys. Res.*, *99*, 5475–5485.

Collins, R. L., X. Tao, and C. S. Gardner (1996), Gravity wave activity in the upper mesosphere over Urbana, Illinois: Lidar observations and analysis of gravity wave propagation models, *J. Atmos. Terr. Phys.*, *58*, 1905–1926.

Collins, R. L., D. Thorsen, and S. J. Franke (1997), Comparative MF radar and Na lidar measurements of fluctuating winds in the mesopause region, *J. Geophys. Res.*, *102*, 16,583–16,591.

Dewan, E. M., and R. E. Good (1986), Saturation and the "universal" spectrum for vertical profiles of horizontal scalar winds in the atmosphere, *J. Geophys. Res.*, *91*, 2742–2748.

Franke, P. M., and R. L. Collins (2003), Evidence of gravity wave breaking in lidar data from the mesopause region, *Geophys. Res. Lett.*, *30*(4), 1155, doi:10.1029/2001GL014477.

Fritts, D. C., and M. J. Alexander (2003), Gravity wave dynamics and effects in the middle atmosphere, *Rev. Geophys.*, *41*(1), 1003, doi:10.1029/2001RG000106.

Gardner, C. S., and A. Z. Liu (2007), Seasonal variations of vertical fluxes of heat and horizontal momentum in the mesopause region at Starfire Optical Range, New Mexico, *J. Geophys. Res.*, *112*, D09113, doi:10.1029/2005JD006179.

Gardner, C. S., and M. J. Taylor (1998), Observational limits for lidar, radar, and airglow imager measurements of gravity wave parameters, *J. Geophys. Res.*, *103*, 6427–6437.

Gardner, C. S., and D. G. Voelz (1987), Lidar studies of the nighttime sodium layer over Urbana, Illinois, 2. Gravity waves, *J. Geophys. Res.*, *92*, 4673–4693.

Gardner, C. S, Y. Zhao, and A. Z. Liu (2002), Atmospheric stability and gravity wave dissipation in the mesopause region, *J. Atmos. Sol. Terr. Phys.*, *64*, 923–929.

Gavrilov, N. M., and S. Fukao (1999), A comparison of seasonal variations of gravity wave intensity observed by the MU radar with a theoretical model, *J. Atmos. Sci.*, *56*, 3485–3494.

Gavrilov, N. M., and C. Jacobi (2004), A study of seasonal variations of gravity wave intensity in the lower thermosphere using LF D1 wind observations and a numerical model, *Ann. Geophys.*, *22*, 35–45.

Gavrilov, N. M., D. M. Riggin, and D. C. Fritts (2003), Medium-frequency radar studies of gravity-wave seasonal variations over Hawaii (22°N, 160°W), *J. Geophys. Res.*, *108*(D20), 4655, doi:10.1029/2002JD003131.

Gibson-Wilde, D. E., I. M. Reid, S. D. Eckermann, and R. A. Vincent (1996), Simulation of lidar measurements of gravity waves in the mesosphere, *J. Geophys. Res.*, *101*, 9509–9522.

Hickey, M. P., and J. M. C. Plane (1995), A chemical-dynamical model of wave-driven sodium fluctuations, *Geophys. Res. Lett.*, *22*, 2861–2864.

Hines, C. O. (1991), The saturation of gravity waves in the middle atmosphere. Part II: Development of Doppler-spread theory, *J. Atmos. Sci.*, *48*, 1360–1379.

Li, T., C. Y. She, H.-L. Liu, and M. Montgomery (2007), Evidence of a gravity wave breaking event and the estimation of the wave characteristics from sodium lidar observation over Fort Collins, CO (41°N, 105°W), *Geophys. Res. Lett.*, *34*, L05815, doi:10.1029/2006GL028988.

Liu, A. Z., and C. S. Gardner (2005), Vertical heat and constituent transport in the mesopause region by dissipating gravity waves at Maui, Hawaii (20.7°N), and Starfire Optical Range, New Mexico (35°N), *J. Geophys. Res.*, *110*, D09S13, doi:10.1029/2004JD004965.

Nappo, C. J. (2002), *An Introduction to Atmospheric Gravity Waves*, Academic, San Diego, Calif.

Reisin, E. R., and J. J. Scheer (2004), Gravity wave activity in the mesopause region from airglow measurements at El Leoncito, *J. Atmos. Sol. Terr. Phys.*, *66*, 655–661.

Senft, D. C., and C. S. Gardner (1991), Seasonal variability of gravity wave activity and spectra in the mesopause region at Urbana, *J. Geophys. Res.*, *96*, 17,229–17,264.

She, C. Y., J. R. Yu, H. Latifi, and R. E. Bills (1992), High-spectral-resolution fluorescence lidar for mesospheric sodium temperature measurements, *Appl. Opt.*, *31*, 2095–2106.

Swenson, G. R., A. Z. Liu, and J. Tang (2003), High frequency atmospheric gravity wave damping in the mesosphere, *Adv. Space Res.*, *32*, 785–793.

Vanzandt, T. E. (1982), A universal spectrum of buoyancy waves in the atmosphere, *Geophys. Res. Lett.*, *9*, 575–578.

Vincent, R. A. (1994), Gravity-wave motions in the mesosphere and lower thermosphere observed at Mawson, Antarctica, *J. Atmos. Terr. Phys.*, *56*, 593–602.

Williams, B. P., M. A. White, D. A. Krueger, and C. Y. She (2002), Observation of a large amplitude wave and inversion layer leading to convective instability in the mesopause region over Fort Collins, CO (41°N, 105°W), *Geophys. Res. Lett.*, *29*(17), 1850, doi:10.1029/2001GL014514.

Xu, J., and A. K. Smith (2003), Perturbations of the sodium layer: Controlled by chemistry or dynamics?, *Geophys. Res. Lett.*, *30*(20), 2056, doi:10.1029/2003GL018040.

Xu, J., A. K. Smith, R. L. Collins, and C.-Y. She (2006), Signature of an overturning gravity wave in the mesospheric sodium layer: Comparison of a nonlinear photochemical-dynamical model and lidar observations, *J. Geophys. Res.*, *111*, D17301, doi:10.1029/2005JD006749.

Yang, G., B. Clemesha, P. Batista, and D. Simonich (2006), Gravity wave parameters and their seasonal variations derived from Na lidar observations at 23°S, *J. Geophys. Res.*, *111*, D21107, doi:10.1029/2005JD006900.

Yang, G., B. Clemesha, P. Batista, and D. Simonich (2008a), Lidar study of the characteristics of gravity waves in the mesopause region at a southern low-latitude location, *J. Atmos. Sol. Terr. Phys.*, *70*, 991–1011.

Yang, G., B. Clemesha, P. Batista, and D. Simonich (2008b), Improvement in the technique to extract gravity wave parameters from lidar data, *J. Geophys. Res.*, *113*, D19111, doi:10.1029/2007JD009454.

Yu, R., and C. Y. She (1993), Lidar-observed temperature structures and gravity-wave perturbations of the mesopause region in the springs of 1990–1992 over Fort Collins, CO, *Appl. Phys. B*, *57*, 231–238.

P. Batista, B. Clemesha, D. Simonich, and G. Yang, Instituto Nacional de Pesquisas Espaciais, São José dos Campos, 23337-010 SP, Brazil. (yyyguotao@hotmail.com)